# An accurate treatment of non-homogeneous boundary conditions for development of the BEM

A. Romero[a,*], P. Galvín[a], A. Tadeu[b,c]

[a]*Escuela Técnica Superior de Ingeniería, Universidad de Sevilla, Camino de los Descubrimientos, 41092 Sevilla, Spain*
[b]*ITeCons - Institute for Research and Technological Development in Construction, Energy, Environment and Sustainability, Rua Pedro Hispano s/ n., 3030-289 Coimbra, Portugal*
[c]*ADAI - LAETA, Department of Civil Engineering, University of Coimbra, Pólo II, Rua Luís Reis Santos, 3030-788 Coimbra, Portugal*

**Abstract**

This paper proposes an enhancement of the treatment of non-homogeneous boundary conditions to improve the boundary element method (BEM) formulation. The standard formulation is modified by introducing the boundary conditions in the integral kernels. The boundary conditions are implicitly defined through known parameters depending on the geometry, rather than by prescribing nodal values as is done in the standard formulation. The main advantage of this procedure is that the right-hand side of the system of equations is integrated taking the exact distribution of loads into account. This approach is implemented in the Bézier-Bernstein space to yield a geometry-independent field approximation. We use the Bézier-Bernstein form of a polynomial as an approximation basis to represent both geometry and field variables. The application of the proposed method covers the resolution of complex boundary value problems as optimization with uncertain data, material modelling with graded impedance, and the definition of general boundary constraints. The performance of the proposed method is shown by solving the Helmholtz equation in two dimensions. The proposed method is numerically compared to the standard BEM formulation in two benchmark problems. Finally, the application of complex impedance boundary conditions is analysed in a numerical example.

*Keywords:* Boundary conditions; Element approximation; Computer-aided design; Bézier curve; Bernstein polynomial; Acoustic impedance.

## 1. Introduction

Of the wide range of numerical methods, the most popular are the finite element method (FEM), the finite difference method (FDM) and the boundary element method (BEM). However, the BEM has a distinctive role as a boundary method, as opposed to FEM and FDM, as noted by Cheng and Cheng [1]. Owing to its

*Corresponding author
*Email address:* aro@us.es (A. Romero)

higher accuracy and efficiency, the BEM has been widely used in many engineering fields such as acoustics scattering, fracture mechanics, and soil wave propagation.

The BEM is a collocation method that uses the fundamental solution to a problem as a weighted function [2]. The starting point for the formulation of the BEM is the boundary integral equation (BIE), which can be deduced from the weighted residual method, Green's third identity or Betti's reciprocal theorem. The boundary is then discretised into elements where the unknown values of the field variables coincide with the nodal positions. The field variables are usually approximated by nodal values that have a clear physical meaning. Typically, the element approximation involves a linear combination of nodal values and interpolation functions.

Once the element approximation is introduced, we find that the BIE cannot be satisfied exactly unless the approximation of the field variables is exact [3]. This induces an error that determines the accuracy of the method, as will be discussed later. The concept of residual is introduced to represent the error by non-achievement of the integral representation. The collocation method is then used to require that the residual vanishes at a set of points called collocation points [4].

These points are usually chosen to be coincident with nodes and this procedure then yields to a non-symmetric linear system of equations that relates the nodal variables. It proceeds by applying the necessary constraints for the solution of the boundary value problem. Typically, the system of equations is rearranged by moving the columns of the influence matrix according to the boundary conditions. The right-hand side of the system of equations is computed by multiplying those columns by the nodal values of the field variables.

Some recent applications of the BEM regarding the reliability analysis coincided with the importance of achieving accurate and efficient numerical solutions [5–10]. Accordingly, Vable [11] discussed the various sources of errors in BEM that were classified as: *i*) formulation error, *ii*) interpolation error, *iii*) integration error, *iv*) continuity error, *v*) collocation error, *vi*) matrix conditioning error, and *vii*) mesh error.

The interpolation error is one of the most important sources of error in BEM analysis [12] because of a lack of precision in the geometry discretisation and the field variables approximation. The loss of accuracy in the model discretisation is mainly given by the difficulty to represent the field variables through a polynomial approximation. Hence, many authors have conducted improvements related to geometry representation and field approximation. These studies covered the parametric representation of the geometry [13, 14], the isogeometric approach [15, 16], and the spectral formulations [17–20]. These publications have led to progress in the formulation of the BEM.

This article presents an improvement in the treatment of boundary conditions based on the idea of developing a reliable method for engineering analysis. The novelty of the proposed method lies in the modification of BEM integral kernels to include the actual distribution of the boundary conditions instead of the polynomial approximation used in the standard BEM formulation. Therefore, these terms of the integral representation related to known values of the field variables are satisfied exactly since the exact

distribution given by boundary conditions is considered.

The proposed method has been implemented in the BEM formulation based on the Bézier-Bernstein space [21] to consider the exact boundary geometry. Also, this formulation allows the use of arbitrary high-order elements. Thus, the proposed method presents some enhancements according to Reference [11]: *i*) low interpolation error due to the use of high-order elements, *ii*) the collocation error is reduced because the boundary conditions are implicit at the integration kernels, and *iii*) no mesh error since exact CAD model geometry is considered.

The outline of the paper is as follows. In Section 2, the definition of boundary conditions in the BEM is presented and the Bézier-Bernstein space is briefly described. The proposed method is verified in Section 3 from two benchmark problems with a known analytical solution. A numerical example is presented and investigated in Section 4. Finally, the main results drawn from this research are summarised in the Conclusion section.

## 2. Numerical model

In this work, we consider the Helmholtz equation, without loss of generality, to present the proposed formulation. The governing equation in the bounded domain $\Omega$ with the piecewise smooth boundary $\Gamma$ defined by its normal outward $\mathbf{n}(\mathbf{x})$ is:

$$\nabla^2 u(\mathbf{x}) + \kappa^2 u(\mathbf{x}) = 0, \qquad \mathbf{x} \in \Omega, \tag{1}$$

where $u(\mathbf{x})$ is the velocity potential and $\kappa > 0$ denotes the wavenumber. The problem definition is completed by setting the boundary conditions for on $\Gamma = \partial\Omega$. Dirichlet and Neumann boundary conditions are defined as $u(\mathbf{x}) = \overline{u}(\mathbf{x})$ and $q(\mathbf{x}) = \partial u(\mathbf{x})/\partial \mathbf{n}(\mathbf{x}) = \overline{q}(\mathbf{x})$, respectively. Also, it is possible to adopt the Robin boundary condition to gather the three types of boundary conditions in one expression:

$$\alpha(\mathbf{x})u(\mathbf{x}) + \beta(\mathbf{x})q(\mathbf{x}) = \gamma(\mathbf{x}), \qquad \mathbf{x} \in \Gamma, \tag{2}$$

where $\alpha(\mathbf{x})$, $\beta(\mathbf{x})$ and $\gamma(\mathbf{x})$ are known parameters along the boundary that allow the following definitions:

$$\beta(\mathbf{x}) = 0: \qquad u(\mathbf{x}) = \overline{u}(\mathbf{x}) = \gamma(\mathbf{x})/\alpha(\mathbf{x}) \qquad \text{Dirichlet boundary condition} \tag{3}$$

$$\alpha(\mathbf{x}) = 0: \qquad q(\mathbf{x}) = \overline{q}(\mathbf{x}) = \gamma(\mathbf{x})/\beta(\mathbf{x}) \qquad \text{Neumann boundary condition} \tag{4}$$

$$\alpha(\mathbf{x}) \neq 0,\ \beta(\mathbf{x}) \neq 0: \qquad q(\mathbf{x}) = \overline{q}(\mathbf{x}) = (\gamma(\mathbf{x}) - \alpha(\mathbf{x})u(\mathbf{x}))/\beta(\mathbf{x}) \qquad \text{Robin boundary condition} \tag{5}$$

We can see from the above definitions that the Neumann condition is a particular case of the Robin type when $\alpha(\mathbf{x}) = 0$. Therefore, it is not necessary to distinguish between the two types of boundary conditions in the problem definition. Then, the boundary is defined as $\Gamma = \Gamma^u \bigcup \Gamma^q$ according to the following definitions:

$$u(\mathbf{x}) = \overline{u}(\mathbf{x}) = \gamma(\mathbf{x})/\alpha(\mathbf{x})\,, \qquad \mathbf{x} \in \Gamma^u\,, \tag{6}$$

$$q(\mathbf{x}) = \overline{q}(\mathbf{x}) = (\gamma(\mathbf{x}) - \alpha(\mathbf{x})u(\mathbf{x}))/\beta(\mathbf{x})\,, \qquad \mathbf{x} \in \Gamma^q\,. \tag{7}$$

It is assumed that $\kappa^2$ is not an eigenvalue of $\nabla^2 u(\mathbf{x}) + \kappa^2 u(\mathbf{x}) = 0$ subject to the homogeneous form of the imposed boundary conditions.

### *2.1. Boundary element formulation*

The basic integral equation is the starting point as we introduced before, which can be written as follows [22]:

$$c(\xi)u(\xi) = \int_\Gamma \left( \frac{\partial u(\mathbf{x})}{\partial \mathbf{n}(\mathbf{x})} \Psi(\mathbf{x},\xi) - u(\mathbf{x}) \frac{\partial \Psi(\mathbf{x},\xi)}{\partial \mathbf{n}(\mathbf{x})} \right) d\Gamma(\mathbf{x})\,, \tag{8}$$

where $\xi$ is the collocation point, $q(\mathbf{x}) = \partial u(\mathbf{x})/\partial \mathbf{n}(\mathbf{x})$ is the normal flux, $\Psi(\mathbf{x},\xi)$ is the fundamental solution (the Hankel function $H_0^{(1)}(\kappa|\mathbf{x}-\xi|)$) at point $\mathbf{x}$ due to a point source located at $\xi$, and the integral-free term $c(\xi)$ depends only on the boundary geometry at the collocation point $\xi$. The dependence on the wavenumber $\kappa$ has been omitted intentionally in the above equation for simplicity of notation.

The basic integral representation implies that the potential $u(\xi)$ is obtained by integrating the field variables $u(\mathbf{x})$ and $q(\mathbf{x})$ over the boundary $\Gamma$, weighted by the fundamental solution $\Psi(\mathbf{x},\xi)$. Typically, the accuracy in the computation of $u(\xi)$ depends on the approximation of the field variables at the boundary, and it is also conditioned by the precision of the integration scheme to solve Equation (8). The accuracy in the computation of $u(\xi)$ will only rely on the precision of the quadrature rule when the field variables represent the actual solution at the boundary. This topic is discussed below.

Following the scheme depicted in section 1, the boundary is discretised into $N$ elements with $\Gamma = \bigcup_{j=1}^{N} \Gamma^j$. Thus, Equation (8) is rewritten as follows:

$$c(\xi)u(\xi) = \sum_{j=1}^{N} \int_{\Gamma^j} \left( \frac{\partial u(\mathbf{x})}{\partial \mathbf{n}(\mathbf{x})} \Psi(\mathbf{x},\xi) - u(\mathbf{x}) \frac{\partial \Psi(\mathbf{x},\xi)}{\partial \mathbf{n}(\mathbf{x})} \right) d\Gamma\,. \tag{9}$$

Equation (9) represents the discretised basic integral representation for $u(\xi)$, which is computed as a piece-wise integration of the field variables over the boundary. The field variables within an element $\Gamma^j$ are interpolated from the nodal values $u^k$ using element shape functions $\phi^k(\mathbf{x})$ of order $p$:

$$u(\mathbf{x}) = \sum_{i=0}^{p} \phi^i(\mathbf{x}) u^i = \boldsymbol{\phi}(\mathbf{x}) \mathbf{u}^e\,. \tag{10}$$

Then, the element approximation is substituted into Equation (9) to yield the following expression:

$$c(\xi)u(\xi) = \sum_{j=1}^{N} \left[ \left( \int_{\Gamma^j} \boldsymbol{\phi}(\mathbf{x}) \Psi(\mathbf{x},\xi)\, d\Gamma \right) \frac{\partial \mathbf{u}^e}{\partial \mathbf{n}} - \left( \int_{\Gamma^j} \boldsymbol{\phi}(\mathbf{x}) \frac{\partial \Psi(\mathbf{x},\xi)}{\partial \mathbf{n}(\mathbf{x})}\, d\Gamma \right) \mathbf{u}^e \right]\,. \tag{11}$$

In this case, the basic integral Equation (11) differs from Equation (9) because the potential $u(\xi)$ is given by integration of field nodal values interpolated by the element shape functions. The accuracy is constrained by the element approximation and should be lower than in Equation (9), even if $\mathbf{u}^e$ takes the exact value of the field variable $u(\mathbf{x})$ at nodal positions unless the element approximation of the field variables is exact. Therefore, the element approximation implies a loss of accuracy in the evaluation of the integral representation.

Finally, the collocation method allows the definition of a system of equations that relates nodal values $\mathbf{u}$ and $\mathbf{q}$ over the boundary:

$$\mathbf{H}\mathbf{u} = \mathbf{G}\mathbf{q}\,, \tag{12}$$

where $\mathbf{H}$ and $\mathbf{G}$ are the fully non-symmetrical boundary element system matrices. After boundary condition have been prescribed, Equation (12) is rewritten as $\mathbf{A}\mathbf{X} = \mathbf{b}$ [23], where $\mathbf{A}$ is the matrix of coefficients, $\mathbf{X}$ collects the unknown nodal values, and $\mathbf{b}$ is the right-hand side.

Our concern begins with the approximation of the right-hand side of the system of equations. This term is computed from the rearrangement of Equation (11) according to the boundary conditions, as:

$$\mathbf{b}(\xi) = \sum_{\Gamma^j \in \Gamma^q} \left( \int_{\Gamma^j} \boldsymbol{\phi}(\mathbf{x}) \Psi(\mathbf{x}, \xi)\, d\Gamma \right) \frac{\partial \overline{\mathbf{u}}^e}{\partial \mathbf{n}} - \sum_{\Gamma^j \in \Gamma^u} \left( \int_{\Gamma^j} \boldsymbol{\phi}(\mathbf{x}) \frac{\partial \Psi(\mathbf{x}, \xi)}{\partial \mathbf{n}(\mathbf{x})}\, d\Gamma \right) \overline{\mathbf{u}}^e\,, \tag{13}$$

where $\Gamma^u$ and $\Gamma^q$ denote those parts of the boundary where Dirichlet and Robin (or Neumann) conditions are respectively defined. In this equation, the element approximation is used to interpolate the field variable $\overline{u}(\mathbf{x})$, and its derivative, through the nodal value $\overline{\mathbf{u}}^e$ and the element shape functions $\boldsymbol{\phi}(\mathbf{x})$. Following this procedure, the boundary conditions are prescribed as known nodal values, but the approximation of the field variables through element shape function implies a loss of accuracy in the collocation method, as we mentioned above. Therefore, this approach does not seem to be sufficiently justified for the application of boundary conditions, given that the distribution of field variables is fully known.

The novelty of the proposed method derives from this lack of accuracy. Thus, the actual distribution of $\overline{u}(\mathbf{x})$ is included in the integration kernels of Equation (13). Moreover, the definition of boundary conditions given by Equation (2) is used to develop a more general method. The basic integral representation of $u$ given by Equation (9) is modified as follows, according to the boundary conditions given by Equation (2):

$$\begin{aligned} c(\xi)u(\xi) = & \sum_{\Gamma^j \in \Gamma^u} \int_{\Gamma^j} \frac{\partial u(\mathbf{x})}{\partial \mathbf{n}(\mathbf{x})} \Psi(\mathbf{x}, \xi)\, d\Gamma - \sum_{\Gamma^j \in \Gamma^u} \int_{\Gamma^j} \frac{\gamma(\mathbf{x})}{\alpha(\mathbf{x})} \frac{\partial \Psi(\mathbf{x}, \xi)}{\partial \mathbf{n}(\mathbf{x})}\, d\Gamma \\ & - \sum_{\Gamma^j \in \Gamma^q} \int_{\Gamma^j} \left( \frac{\alpha(\mathbf{x})}{\beta(\mathbf{x})} \Psi(\mathbf{x}, \xi) + \frac{\partial \Psi(\mathbf{x}, \xi)}{\partial \mathbf{n}(\mathbf{x})} \right) u(\mathbf{x})\, d\Gamma + \sum_{\Gamma^j \in \Gamma^q} \int_{\Gamma^j} \frac{\gamma(\mathbf{x})}{\beta(\mathbf{x})} \Psi(\mathbf{x}, \xi)\, d\Gamma\,. \end{aligned} \tag{14}$$

Once the element approximation given by Equation (10) is introduced in the above equation, it becomes:

$$
\begin{aligned}
& c(\xi)u(\xi) - \sum_{\Gamma^j \in \Gamma^u} \left( \int_{\Gamma^j} \boldsymbol{\phi}(\mathbf{x}) \Psi(\mathbf{x}, \xi)\, d\Gamma \right) \frac{\partial \mathbf{u}^e}{\partial \mathbf{n}} \\
& + \sum_{\Gamma^j \in \Gamma^q} \left\{ \int_{\Gamma^j} \left( \frac{\alpha(\mathbf{x})}{\beta(\mathbf{x})} \Psi(\mathbf{x}, \xi) + \frac{\partial \Psi(\mathbf{x}, \xi)}{\partial \mathbf{n}(\mathbf{x})} \right) \boldsymbol{\phi}(\mathbf{x})\, d\Gamma \right\} \mathbf{u}^e \\
& = \sum_{\Gamma^j \in \Gamma^q} \int_{\Gamma^j} \frac{\gamma(\mathbf{x})}{\beta(\mathbf{x})} \Psi(\mathbf{x}, \xi)\, d\Gamma - \sum_{\Gamma^j \in \Gamma^u} \int_{\Gamma^j} \frac{\gamma(\mathbf{x})}{\alpha(\mathbf{x})} \frac{\partial \Psi(\mathbf{x}, \xi)}{\partial \mathbf{n}(\mathbf{x})}\, d\Gamma \,.
\end{aligned}
\tag{15}
$$

Equation (15) has been rearranged according to the boundary conditions. It should be noticed that the right-hand side of this equation does not depend on the element approximation and, therefore, higher accuracy than a standard formulation is expected. After all known $u(\xi)$ for $\xi$ belonging to $\Gamma^u$ are passed to the right-hand side, the following system of equations is obtained:

$$
\mathbf{A}\mathbf{X} = \mathbf{b} \,. \tag{16}
$$

The solution for the system of equations gives unknown nodal values of $u(\mathbf{x})$ and $q(\mathbf{x})$ at the boundary. Afterwards, the potential $u(\xi)$ at internal point $\xi$ in the domain $\Omega$ can be computed from Equation (15), making the free term $c(\xi) = 1$. The solution at internal points also benefits from the proposed treatment of the boundary conditions.

This approach has the following advantages over the standard BEM formulation: *i*) the computation of the right-hand side is independent of the element approximation; and *ii*) the Robin boundary condition is implicitly considered in the element matrix through parameters $\alpha(\mathbf{x})$, $\beta(\mathbf{x})$ and $\gamma(\mathbf{x})$ keeping the spatial information, instead of a relationship between nodal variables as is done in the standard BEM formulation. Therefore, the proposed method has high accuracy as will be shown in the next section.

Although the proposed method is valid for any BEM formulation, it is implemented in the BEM formulation based on the Bézier-Bernstein space [21] to show its capabilities. The next section summarises the main ideas for the method.

### *2.2. The BEM formulation in the Bézier-Bernstein space*

The Bézier-Bernstein space is used to describe the exact boundary geometry and to approximate the field variables. It is based on the application of polynomials in Bernstein form, that grows with the development of Bézier curves $\mathbf{r}_n(t)$ in computer-aided design.

The Bézier curve is defined over the interval $t \in [0, 1]$ as:

$$
\mathbf{r}_n(t) = \sum_{k=0}^{n} \mathbf{b}_k B_k^n(t), \tag{17}
$$

where $\mathbf{b}_k$ are the control points used to approximate the geometry and $n$ the curve degree. The de Casteljau algorithm is often used for evaluating and splitting a Bézier curve $\mathbf{r}_n(t)$ at a given point $t$ [24]. Although

the de Casteljau algorithm allows an easy evaluation of a Bézier curve, it is computationally expensive. An efficient curve computation is achieved using the polar form (or blossom) of a Bézier curve $\mathbf{r}_n(t)$ [25], which defines a multi-affine transformation satisfying:

$$\mathbf{b}_k = \mathbf{R}(\underbrace{0,\ldots,0}_{n-k},\underbrace{1,\ldots,1}_{k}), \tag{18}$$

where $\mathbf{R}(t_1,\ldots,t_n)$ is computed as:

$$\mathbf{R}(t_1,\ldots,t_n) = \sum_{\substack{I\cap J=\emptyset \\ I\cup J=\{1,2,\ldots,n\}}} \prod_{i\in I}(1-t_i)\prod_{j\in J} t_j \mathbf{b}_{|J|}. \tag{19}$$

Thus, a polynomial in Bernstein form can be formulated in the polar form, substituting Equation (18) into Equation (17) as follows:

$$\mathbf{r}_n(t) = \sum_{k=0}^{n} \mathbf{R}(\underbrace{0,\ldots,0}_{n-k},\underbrace{1,\ldots,1}_{k}) B_k^n(t) = \mathbf{R}(t,\ldots,t). \tag{20}$$

The Bézier-Bernstein space is used to describe the exact element geometry as $\Gamma^j(\mathbf{x}) = \mathbf{r}_n^j(t)$. Hence, the element integrals in Equation (15) are rewritten in the univariate basis $t \in [0,1]$ as [21, 26]:

$$\int_{\Gamma^j} f(\mathbf{x},\xi)\, d\Gamma = \int_0^1 f(\mathbf{x}(t),\xi) \left|\frac{d\mathbf{r}_n^j(t)}{dt}\right| dt, \tag{21}$$

where $f(\mathbf{x},\xi)$ represents the integration kernels. Moreover, Equation (21) can be transformed into the integration interval $[-1,1]$ to employ a Gauss-Legendre quadrature.

Moreover, the proposed method employs the Lagrange interpolant relative to the Bernstein basis for the field variable approximation to an element [27]. The field approximation given by Equation (10) interpolates $n+1$ nodal values through the element shape functions $P_n^i = \phi^i$ of order $n$, for $i = 0,\ldots,n$. The proposed element is defined by the nodal positions $t_j$ in the univariate basis. The Lagrange interpolant $P_n^i$ derived from the Bernstein basis must fulfil the following condition at element nodes $t_j$:

$$P_n^i(t_j) = \phi^i(t_j) = \sum_{k=0}^{n} c_k B_k^n(t_j) = \delta_{ij}, \qquad j = 0,\ldots,n, \tag{22}$$

where, $c_k$ are the control points used to define the Lagrange polynomial $P_n^i$. This condition is commonly expressed as a linear system of equations through the Bernstein-Vandermonde matrix $A_{ij} = B_i^n(t_j)$ as:

$$\begin{bmatrix} B_0^n(t_0) & B_1^n(t_0) & \dots & B_k^n(t_0) & \dots & B_n^n(t_0) \\ B_0^n(t_1) & B_1^n(t_1) & \dots & B_k^n(t_1) & \dots & B_n^n(t_1) \\ \dots & & & & & \\ B_0^n(t_i) & B_1^n(t_i) & \dots & B_k^n(t_i) & \dots & B_n^n(t_i) \\ \dots & & & & & \\ B_0^n(t_n) & B_1^n(t_n) & \dots & B_k^n(t_n) & \dots & B_n^n(t_n) \end{bmatrix} \begin{Bmatrix} c_0^i \\ c_1^i \\ \dots \\ c_k^i \\ \dots \\ c_n^i \end{Bmatrix} = \begin{Bmatrix} 0 \\ 0 \\ \dots \\ 1 \\ \dots \\ 0 \end{Bmatrix}. \tag{23}$$

Thus, the element shape function $\phi^i$ is defined by control points obtained from the solution of (23).

Then, the field approximation given by Equation (10) in the univariate basis $t$ becomes:

$$u(t) = \sum_{i=0}^{p} \phi^i(t) u^i = \sum_{i=0}^{p} \left\{ \sum_{k=0}^{n} c_k^k B_k^n(t) \right\} u^i = \sum_{i=0}^{p} R^i(t, \dots, t) u^i, \tag{24}$$

where the evaluation of the element shape function $\phi^i(t)$ also benefits from the computational advantages of using the polar form $R^i(t_1, \dots, t_n)$ according to Equation (19).

Once the geometry and the field approximation given by Equations (20) and (24) are introduced in Equation (15), the boundary integrals are computed using a standard Gauss-Legendre quadrature with $p+1$ integration points whenever the collocation point is sufficiently distant from the integration element. Otherwise, the solution of singular or weakly singular integrals is numerically computed using a smoothing transformation using a Gauss-Legendre quadrature [28].

Figure 1 shows a scheme for the treatment of singular and weakly singular integrals. This figure represents a collocation point $\xi$ and an integration element $\Gamma^j$. The parametric coordinate $t(\xi)$ is found from $\xi$ as the point that minimizes the distance $r(\xi)$ to the integration element. $t(\xi)$ coincides with the coordinate of this node if the collocation point belongs to the integration element. After point $t(\xi)$ has been identified, the element integration is subdivided into two intervals. The element integrals are numerically solved by a smoothing transformation $\varphi_{l,r}(s)$ [28].

We chose a critical radius $r^*$ between the collocation point and the integration element for the identification of singular or nearly singular integrals. Otherwise, the collocation point is sufficiently distant from the integration element and the resulting integrals are regular. The asymptotic behaviour of the fundamental solution is accounted for by selecting the critical radius $r^*$ when the integral becomes singular [21].

## 3. Numerical verification

In this section, we analyse the performance of the proposed method for solving the Helmholtz equation in a square boundary $\Omega := [-1, 1] \times [-1, 1]$ at a high wavenumber $\kappa = 100\,\text{rad/m}$. Four linear Bézier patches were used to define the boundary geometry:

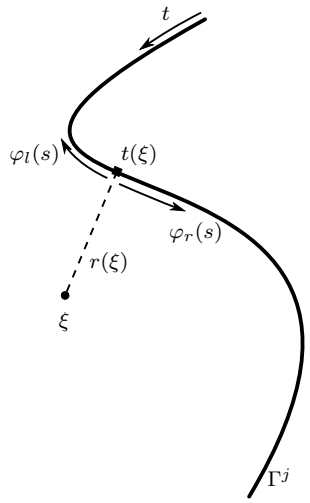


Figure 1: Treatment of singular and weakly singular integral.

$$\Gamma_1 := [-1,1]\times[-1,-1]\,, \Gamma_2 := [1,1]\times[-1,1]\,, \Gamma_3 := [-1,1]\times[1,1]\,, \Gamma_4 := [-1,-1]\times[-1,1]\,. \tag{25}$$

The proposed method was then tested in two benchmark problems. Different boundary conditions were chosen such that the exact solution satisfies $u^I(\mathbf{x}) = \exp(\iota\kappa\mathbf{d}\cdot\mathbf{x})$, where the polarised direction was set to $\mathbf{d} = [1,1]$, and the unit imaginary number was denoted by the Greek letter $\iota$ to prevent confusion with some subscripts used in the paper. Numerical results were compared with a reference solution using the $l_2$ scaled error $\epsilon_2$ to assess the accuracy.

A convergence investigation was carried out for several element lengths $h$ with successive $p-$enrichment. Three different discretisation schemes were tested with element lengths given by $\kappa h = 7.5$, $\kappa h = 3$ and $\kappa h = 1$. The element shape functions were obtained from the interpolation functions defined at Chebyshev points of the first kind [21]. The element order was increased until convergence was reached. For this purpose, we considered that the problem solution was properly approximated if the error satisfied $\log(\epsilon_2(h,p-1)/\epsilon_2(h,p+1)) \leq 1$.

The accuracy of the proposed method was compared with a standard BEM formulation (11). The type of element and the integration scheme was the same in both methods. Only the treatment of boundary conditions was modified.

### *3.1. Example 1*

In this example, Dirichlet and Neumann conditions were prescribed on the boundaries $\Gamma_{1,3}$ and $\Gamma_{2,4}$, respectively. The boundary conditions were prescribed as follows, according to Equation (2):

$$\alpha(\mathbf{x}) = 1\,, \qquad \beta(\mathbf{x}) = 0\,, \qquad \gamma(\mathbf{x}) = u^I(\mathbf{x})\,, \qquad \mathbf{x}\,\text{on}\,\Gamma_{1,3}\,, \tag{26}$$

$$\alpha(\mathbf{x}) = 0\,, \qquad \beta(\mathbf{x}) = 1\,, \qquad \gamma(\mathbf{x}) = \nabla u^I(\mathbf{x}) \cdot \mathbf{n}(\mathbf{x})\,, \qquad \mathbf{x}\,\text{on}\,\Gamma_{2,4}\,. \tag{27}$$

The right-hand side in Equation (15) was computed from the parameters $\alpha(\mathbf{x})$, $\beta(\mathbf{x})$ and $\gamma(\mathbf{x})$ which are included in the integration kernel, as we stated before. Therefore, these terms of the BIE were computed without loss of accuracy due to the element approximation. However, if Equation (13) is considered, the right-hand side of the system of equations is integrated making an approximation of the boundary condition at the nodal position interpolated by the element shape function.

Figure 2 shows the result of the convergence investigation. First, the $l_2$ scaled error $\epsilon_2$ was evaluated over the boundary from the nodal solution. The convergence rate improved as the boundary discretisation became finer in all the studied cases. The proposed method and the standard BEM formulation gave a similar approximation as can be seen Figure 2.(a), with the lowest error $\mathcal{O}(10^{-10})$ being achieved for the finest mesh. However, the accuracy of the two methods in terms of computing the domain solution at the internal point was quite different (Figure 2.(b)). The convergence of the proposed method was much better than in the standard formulation because of the higher accuracy in the right-hand side computation. Moreover, the domain solution was more accurate than the boundary solution since it was computed from the nodal values previously obtained and the prescribed boundary conditions, without any polynomial approximation along with the elements. The lowest error was $\mathcal{O}(10^{-12})$.

For comparison purpose, the potential at the internal point $\xi = (0, 0)$ was computed from the discretised basic integral equation (Equation (9)) using the exact solution for the field variables over the boundary. The solution computed in this way is the best available solution since the BIE was integrated from the exact field distribution. The accuracy of this solution was related to the element order $p$ which defined the number of integration points (see Section 2.2). Therefore, the *hp*-refinement provides a piecewise integration scheme with variable order according to $p$. Figure 2.(b) uses shaded lines to show the computed error. The lowest error was considerably lower than in the previous cases. The proposed method approximated to the best solution particularly for medium and small element lengths. Note that the exact solution $u^I(\mathbf{x})$ has been used to assess the solution at the internal point, instead of the numerical result computed with the BEM, to avoid the inherent inaccuracy of the method.

### *3.2. Example 2*

The second example analyses the ability of the proposed method to represent Robin boundary conditions given by the following expression [29]:

$$\iota\kappa u(\mathbf{x}) + \nabla u(\mathbf{x}) \cdot \mathbf{n}(\mathbf{x}) = g(\mathbf{x})\,, \tag{28}$$

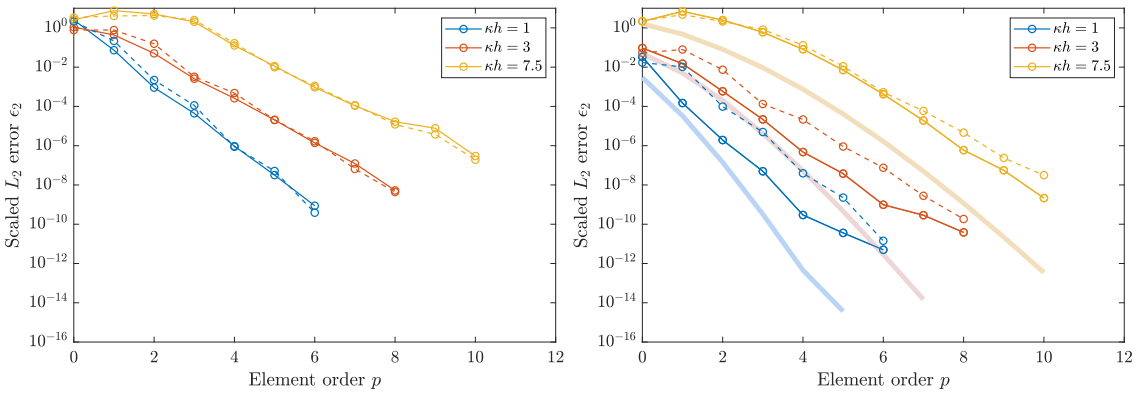


Figure 2: $L_2$ scaled error $\epsilon_2$ for different $\kappa h$ discretisations obtained by the proposed method (solid lines) and a standard BEM (dashed lines): (a) over the boundary, and (b) at the internal point $\xi = (0, 0)$ (the best solution at this point is represented in shaded lines).

where $g(\mathbf{x})$ was chosen accordingly to $u^I(\mathbf{x}) = \exp(\iota\kappa\mathbf{d}\cdot\mathbf{x})$. This condition set the parameters in Equation (2) as follows:

$$\alpha(\mathbf{x}) = \iota\kappa\,, \qquad \beta(\mathbf{x}) = 1\,, \qquad \gamma(\mathbf{x}) = \iota\kappa u^I(\mathbf{x}) + \nabla u^I(\mathbf{x})\cdot\mathbf{n}(\mathbf{x})\,, \qquad \mathbf{x}\in\Gamma\,. \tag{29}$$

The solution computed with the standard BEM was obtained by substituting the flux given by $q(\mathbf{x}) = (g(\mathbf{x}) - \iota\kappa u(\mathbf{x}))$ into Equation (12). This expression gave a node-to-node relationship of the field variables. Then, the system of equations was of the form:

$$(\mathbf{H} + \iota\kappa\mathbf{G})\mathbf{u} = \mathbf{G}\mathbf{g} \tag{30}$$

where $\mathbf{g}$ is a vector that collects the value $g(\xi)$ at each collocation point.

Figure 3 shows the computed errors in both cases. The convergence rates have similar behaviour to that in the above example. In this case, the standard BEM formulation gave a little bit more precision for some cases than the proposed method in the boundary solution, due to the integral kernels' complexity being higher than in the standard formulation. Some additional tests have shown an improvement of the boundary solution by increasing the number of integration points according to the kernel complexity. Once again, the domain solution computed with the proposed method was much better than that obtained by the standard formulation. The discrepancies in the two methods are due to the treatment of boundary conditions in each case. The solution converged to a minimum error $\mathcal{O}(10^{-11})$.

This analysis has depicted the loss of accuracy in the BIE caused by the approximation of boundary conditions from nodal values using element shape functions. The proposed method gave a better approximation than the standard formulation of the BEM, particularly at internal points in the domain. Therefore,

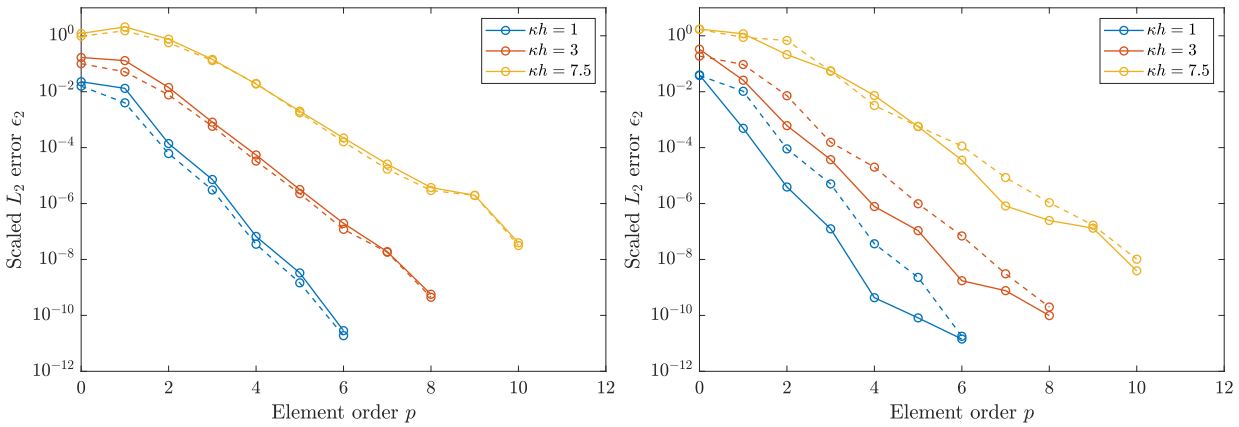


Figure 3: $L_2$ scaled error $\epsilon_2$ for different $\kappa h$ discretisations obtained by the proposed method (solid lines) and a standard BEM (dashed lines): (a) over the boundary, and (b) at the internal point $\xi = (0, 0)$.

it was demonstrated that the proposed treatment of non-homogeneous boundary conditions is suitable for the development of the BEM.

## 4. Numerical example

In this example, we analysed the application of complex impedance boundary conditions. The acoustic impedance is usually defined as a Robin boundary condition given by the relationship $Z = p/v_n$, where $p$ is the sound pressure and $v_n$ the normal particle velocity. This example analyses the effect on the pressure field of rough surfaces with a non-uniform impedance.

We started by studying the wave propagation in a rectangular fluid duct defined by the domain $\Omega := [0, 1] \times [-0.1, 0.1]$ with flat surfaces. The fluid, with density $\rho = 1.225\,\mathrm{kg/m}^3$, allows dilatational waves to propagate with velocity of $c = 340\,\mathrm{m/s}$. The boundary was defined as follows:

$$\Gamma_1 := [0, 0] \times [-0.1, 0.1]\,, \Gamma_2 := [1, 1] \times [-0.1, 0.1]\,, \Gamma_3 := [0, 1] \times [-0.1, -0.1]\,, \Gamma_4 := [0, 1] \times [0.1, 0.1]\,. \quad (31)$$

The boundary $\Gamma_1$ was subjected to a uniform normal velocity $v_n = 1\,\mathrm{m/s}$, while the opposite boundary $\Gamma_2$ had a non-reflecting condition given by $p/v_n = \rho c$. These boundary conditions were approximately equal to set $v_n = 0$ at $\Gamma_{3,4}$. The imposition of boundary conditions at $\Gamma_{3,4}$ is quite straightforward in the proposed method, prescribing $\iota\kappa p(\mathbf{x}) + Z_0 v_n(\mathbf{x}) = 0$, i.e. defining $\alpha(\mathbf{x}) = \iota\kappa$, $\beta(\mathbf{x}) = Z_0$ and $\gamma(\mathbf{x}) = 0$. The problem wavenumber value was $\kappa = 125.7\,\mathrm{rad/m}$ and the characteristic wavelength $\lambda = 0.05\,\mathrm{m}$. This problem has an analytical solution for the one-dimensional (1D) case [30]:

$$p(x) = \rho c \exp(-\iota\kappa x)\,. \quad (32)$$

Figure 4 shows the imaginary part of the pressure field over the boundary and at the domain $\Omega$. The numerical results exhibited an oscillatory behaviour and agreed with the analytical solution. It should be noted that the high impedance value was equivalent to setting a boundary condition $v_n = 0$. Therefore, the numerical result was comparable to the one-dimensional analytical solution.

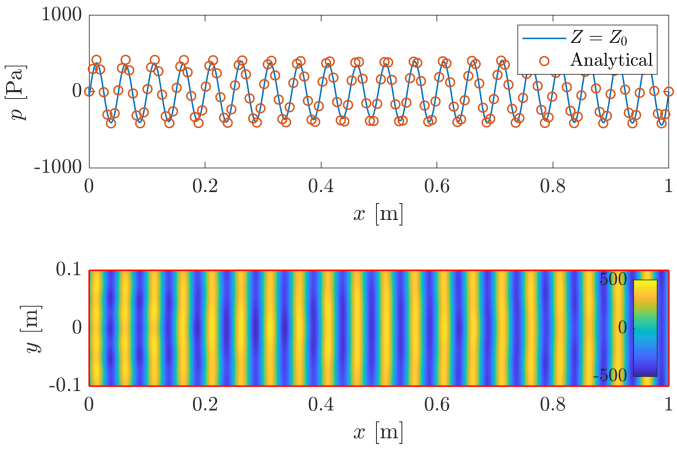


Figure 4: Imaginary part of the pressure field at the boundary (solid line) and in the domain (colour map) for null roughness amplitude. The analytical solution for the 1D case is also shown (circular marks).

Next, the boundary geometry $\Gamma_{3,4}$ was modified by introducing a synthetic rough surface. The roughness measured from the boundary followed a sinusoidal law $r(x) = A_0[1 + \sin(2\pi/T_0 x)]$, where $A_0$ and $T_0$ are the roughness amplitude and period, respectively. Two different roughness periods, $T_0 = 0.4\,\text{m}$ and $T_0 = 0.05\,\text{m}$, and four amplitudes proportionally defined by the wavelength as $A_0 = \{0.2, 0.4, 0.6, 0.8\}\lambda$ were considered.

The geometry was defined using a piecewise third-degree Bézier curve. As an example, Figure 5 shows the duct geometry and its related control polygon for roughness described by periods $T_0 = 0.4\,\text{m}$ and $T_0 = 0.05\,\text{m}$, and the amplitude $A_0 = 0.8\lambda$. The geometry was discretised into elements ensuring that $\kappa h = 3$. The element order $p = 6$ was chosen to ensure twelve nodes per wavelength.

Moreover, a variable impedance was chosen depending on the roughness $r(x)$, varying from $Z_0 = 10^5\,\text{Rayl}$ to $Z_l = 10^2\,\text{Rayl}$ following a linear law $Z(r) = (Z_l - Z_0)r/0.1 + Z_0$ as can be seen in Figure 6. Therefore, the surface impedance decreased as the roughness increased, which could model the effect of loss of stiffness or density decrease of the boundary material.

Figure 6 shows the surface impedance $Z(x)$ for the duct geometries analysed in this example. The maximum impedance $Z_0$ was found in the roughness valleys where $r(x) = 0$. Then, the impedance decreased as the roughness was bigger and exhibited a sinusoidal behaviour.

The accuracy in the application of boundary conditions was ensured since they were included in the integration kernels. Therefore, the problem solution properly accounted for the strong variation of the

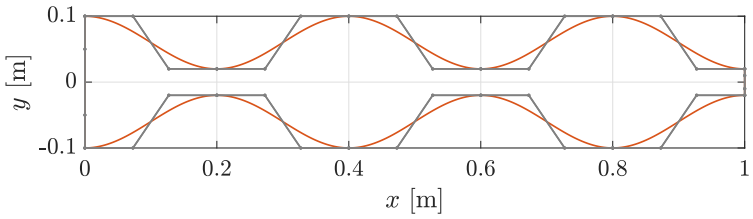


(a)

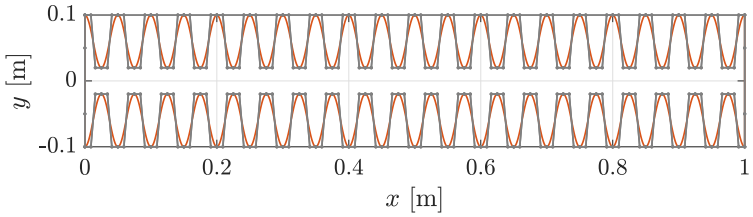


(b)

Figure 5: Duct geometry (red line) and related control polygon (grey line) defined for rough surfaces with periods (a) $T_0 = 0.4\,\mathrm{m}$ and (b) $T_0 = 0.05\,\mathrm{m}$. Roughness amplitude corresponds to $A_0 = 0.8\lambda$.

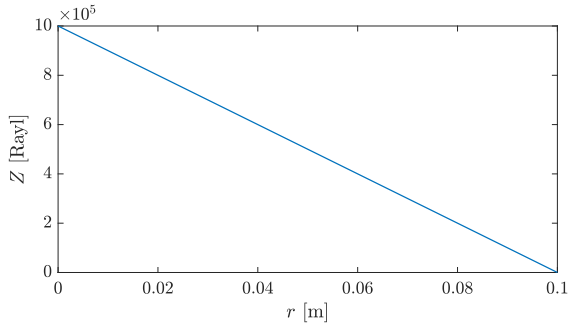


Figure 6: Boundary impedance law dependent on roughness $r(x)$.

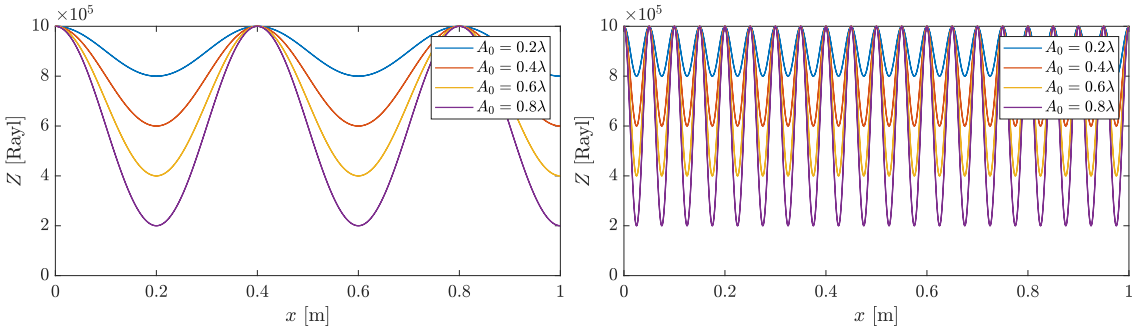


(a) (b)

Figure 7: Boundary impedance for rough surface with periods (a) $T_0 = 0.4\,\mathrm{m}$ and (b) $T_0 = 0.05\,\mathrm{m}$. Roughness amplitude corresponds to $A_0 = \{0.2, 0.4, 0.6, 0.8\}\lambda$.

surface impedance is shown in Figure 7. The model discretisation was done accounting for the wavenumber $\kappa$ but not the complexity of boundary conditions. This is a particular strength of the proposed method.

Figures 8 and 9 show the computed results for characteristics roughness periods $T_0 = 0.4\,\mathrm{m}$ and $T_0 = 0.05\,\mathrm{m}$, respectively, and different roughness amplitude $A_0$. The pressure field at the boundary was compared to that obtained with constant impedance $Z(\mathbf{x}) = Z_0$. The roughness amplitude distorted the pressure field shown for flat surfaces in Figure 4. This effect became clearer as the roughness amplitude was higher and the period shorter. A loss of pressure resulting from changes in the cross-section of the duct was found for roughness amplitudes higher than $A_0 = 0.6\lambda$.

Moreover, we found large differences in pressure at the boundary between the fixed and variable impedance conditions used to solve this problem, and these were more noticeable as the roughness amplitude increased. Therefore, this result justifies the model proposed in this work to address complex boundary conditions. Besides, the formulation of the BEM in the Bézier-Bernstein space allowed us to consider exactly the domain geometry to accurately define the boundary, as can be seen in Figures 5 and 7.

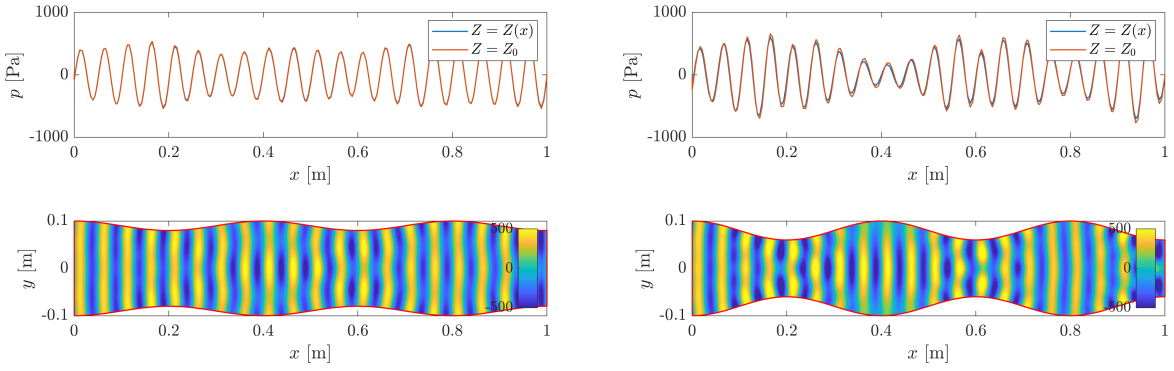


(a) $A_0 = 0.2\lambda$




(b) $A_0 = 0.4\lambda$

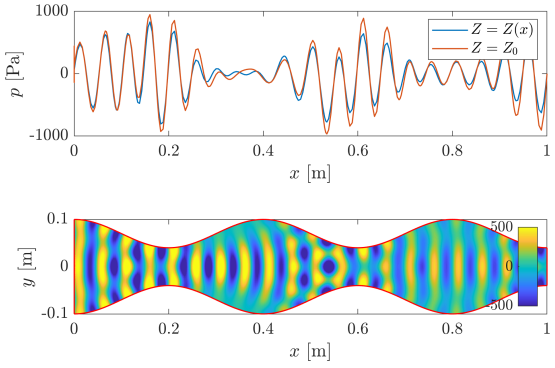


(c) $A_0 = 0.6\lambda$

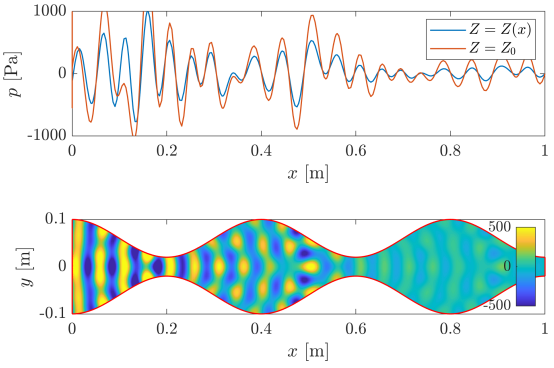


(d) $A_0 = 0.8\lambda$

Figure 8: Imaginary part of the pressure field at the boundary computed from variable impedance (blue line) and fixed impedance (red line) models and over the domain (colour map) for different roughness amplitude $A_0$. The characteristic roughness period is $T_0 = 0.4\,\mathrm{m}$.

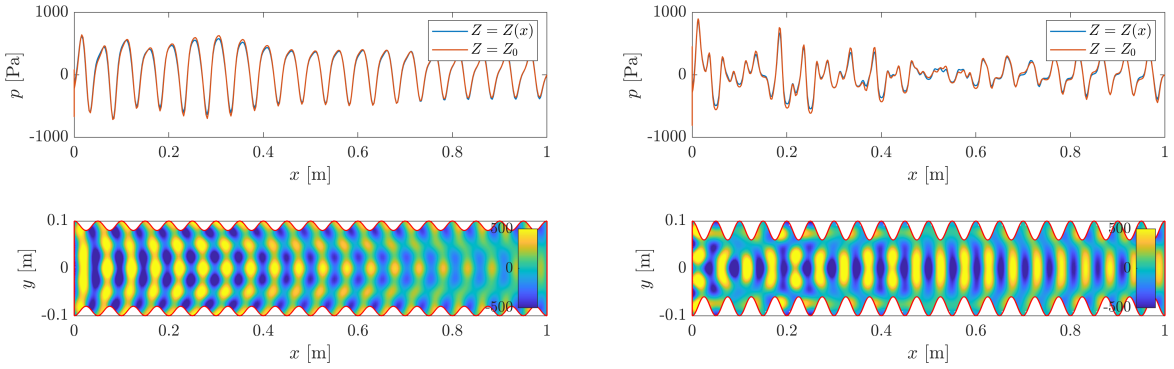


(a) $A_0 = 0.2\lambda$




(b) $A_0 = 0.4\lambda$

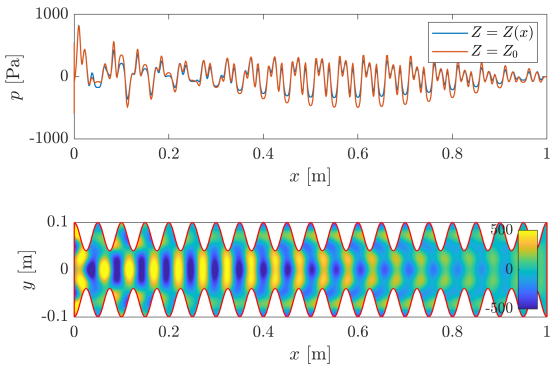


(c) $A_0 = 0.6\lambda$

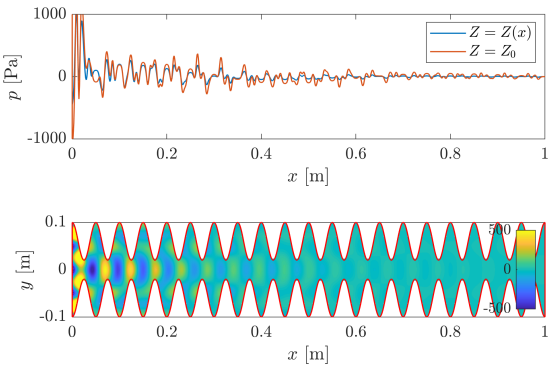


(d) $A_0 = 0.8\lambda$

Figure 9: Imaginary part of the pressure field at the boundary computed from variable impedance (blue line) and fixed impedance (red line) models and over the domain (colour map) for different roughness amplitude $A_0$. The characteristic roughness period is $T_0 = 0.05\,\mathrm{m}$.

## 5. Conclusions

This work has proposed a new treatment of boundary conditions to improve the accuracy of the BEM. The boundary conditions were defined as the type of Dirichlet, Neumann and Robin conditions, using known parameters along the boundary that were included in the integral kernels. This procedure avoided the element approximation and allowed the domain geometry and boundary conditions to be considered exactly in the computation of the right-hand side of the BEM system of equations, as opposed to the standard formulation, which interpolates the boundary conditions from nodal values using the element shape functions. The proposed method was implemented in the BEM formulation based on the Bézier-Bernstein space, which allowed an independent approximation of the geometry and the field variables. However, the method can be extended to other BEM formulations.

The accuracy of the proposed method was demonstrated in two benchmark problems. The results have shown that:

- The discretisation of the basic integral equation defines a piecewise integration when field variables are known. The best solution for an internal domain point is obtained if the field variables achieve the exact solution at the boundary. This means the accuracy depends only on the boundary discretisation and the quadrature rule to compute element integrals. The element approximation of the field variables induces a loss of accuracy related to the element order.

- We have found that the way the BEM prescribes the boundary conditions could be inaccurate. Typically, boundary conditions are directly incorporated into the system of equations, which is obtained from element integration using shape functions. Therefore, the right-hand side has a base error related to the approximation of distributed loads by the element shape functions. The element order improves the precision in the numerical results.

- Although the loss of accuracy can be reduced with a *hp*-refinement, the proposed method yielded better results in the domain than the standard BEM formulation.

A numerical example has been proposed to show the robustness of the proposed method to model complex boundary conditions that are dependent on the geometry. The BEM formulation based on the Bézier-Bernstein space allowed an exact definition of the geometry regardless of the field variable approximation which, in addition to the proposed treatment of the boundary condition, allowed the accurate definition of variable impedance in a duct with a rough surface.

## Acknowledgements

The research work presented was supported by the Spanish Ministry of Economy and Competitiveness (Ministerio de Economía y Competitividad) through research project BIA2016-75042-C2-1-R and by the

Spanish Ministry of Science, Innovation and Universities (Ministerio de Ciencia, Innovación y Universidades) through the scholarship *Salvador de Madariaga* scholarship, Reference PRX19/00298. We are also grateful for support from project POCI-01-0247-FEDER-017759, funded by Portugal 2020 through the Operational Programme for Competitiveness Factors (COMPETE 2020). Financial support is gratefully acknowledged. The authors also wish to acknowledge the support provided by the Andalusian Scientific Computing Centre (CICA).

## References

[1] A.H.-D. Cheng, D.T. Cheng, Heritage and early history of the boundary element method, Engineering Analysis with Boundary Elements 29 (3) (2005) 268–302.

[2] C. Brebbia, J. Domínguez, Boundary Elements An Introductory Course, 1st Edition, WIT Press, 1992.

[3] M. Dehghan, H. Hosseinzadeh, Improvement of the accuracy in boundary element method based on high-order discretization, Computers and Mathematics with Applications 62 (12) (2011) 4461–4471.

[4] M. Schanz, T. Rüberg, L. Kielhorn, Time Domain BEM: Numerical Aspects of Collocation and Galerkin Formulations, Springer Netherlands, Dordrecht, 2009, pp. 415–432.

[5] E.D. Leonel, A. Chateauneuf, W.S. Venturini, P. Bressolette, Coupled reliability and boundary element model for probabilistic fatigue life assessment in mixed mode crack propagation, International Journal of Fatigue 32 (11) (2010) 1823–1834.

[6] C. Su, S. Zhao, H. Ma, Reliability analysis of plane elasticity problems by stochastic spline fictitious boundary element method, Engineering Analysis with Boundary Elements 36 (2) (2012) 118–124.

[7] C. Su, J. Xu, Reliability analysis of Reissner plate bending problems by stochastic spline fictitious boundary element method, Engineering Analysis with Boundary Elements 51 (2015) 37–43.

[8] M.S. Chowdhury, C. Song, W. Gao, C. Wang, Reliability analysis of homogeneous and bimaterial cracked structures by the scaled boundary finite element method and a hybrid random-interval model, Structural Safety 59 (2016) 53–66.

[9] A. Johari, A. Heydari, Reliability analysis of seepage using an applicable procedure based on stochastic scaled boundary finite element method, Engineering Analysis with Boundary Elements 94 (2018) 44–59.

[10] L. Morse, Z. Sharif Khodaei, M.H. Aliabadi, A multi-fidelity boundary element method for structural reliability analysis with higher-order sensitivities, Engineering Analysis with Boundary Elements 104 (2019) 183–196.

[11] M. Vable, Controlling errors in the process of automating boundary element method analysis, Engineering Analysis with Boundary Elements 26 (5) (2002) 405–415.

[12] Z. Zhao, X. Wang, Error estimation and h adaptive boundary elements, Engineering Analysis with Boundary Elements 23 (10) (1999) 793–803.

[13] E. Zieniuk, Bézier curves in the modification of boundary integral equations (BIE) for potential boundary-values problems, International Journal of Solids and Structures 40 (9) (2003) 2301–2320.

[14] E. Zieniuk, K. Szerszeń, Nonelement boundary representation with Bézier surface patches for 3D linear elasticity problems in parametric integral equation system (PIES) and its solving using Lagrange polynomials, Numerical Methods for Partial Differential Equations 34 (1) (2018) 51–79.

[15] R.N. Simpson, S.P.A. Bordas, J. Trevelyan, T. Rabczuk, A two-dimensional Isogeometric Boundary Element Method for elastostatic analysis, Computer Methods in Applied Mechanics and Engineering 209-212 (2012) 87–100.

[16] M.A. Scott, R.N. Simpson, J.A. Evans, S. Lipton, S.P.A. Bordas, T.J.R. Hughes, T.W. Sederberg, Isogeometric boundary element analysis using unstructured T-splines, Computer Methods in Applied Mechanics and Engineering 254 (2013) 197–221.

[17] A.T. Patera, A spectral element method for fluid dynamics: Laminar flow in a channel expansion, Journal of Computational Physics 54 (3) (1984) 468–488.

[18] B. Fornberg, A Practical Guide to Pseudospectral Methods, Cambridge Monographs on Applied and Computational Mathematics, Cambridge University Press, 1996.

[19] U. Iemma, V. Marchese, L. Morino, High-order bem for potential transonic flows, Computational Mechanics 21 (3) (1998) 243–252.

[20] M. Löhndorf, J.M. Melenk, Wavenumber-explicitHp-BEM for high frequency scattering, SIAM Journal on Numerical Analysis 49 (6) (2011) 2340–2363.

[21] A. Romero, P. Galvín, J. Cámara-Molina, A. Tadeu, On the formulation of a BEM in the Bézier–Bernstein space for the solution of Helmholtz equation, Applied Mathematical Modelling 74 (2019) 301 – 319.

[22] T.W. Wu, Boundary Element Acoustics Fundamentals and Computer Codes, Advances in Boundary Elements, WIT Press, 2000.

[23] J. Domínguez, Boundary elements in dynamics, Computational Mechanics Publications and Elsevier Aplied Science, Southampton, 1993.

[24] R.T. Farouki, The Bernstein polynomial basis: A centennial retrospective, Computer Aided Geometric Design 29 (6) (2012) 379–419.

[25] L. Ramshaw, Blossoming: A connect-the-dots approach to splines, Digital Equipment Corporation SRC Report No. 19.

[26] H.-P. Seidel, An introduction to Polar Forms, IEEE Computer Graphics and Applications 13 (1) (1993) 38–46.

[27] R.T. Farouki, T.N.T. Goodman, T. Sauer, Construction of orthogonal bases for polynomials in Bernstein form on triangular and simplex domains, Computer Aided Geometric Design 20 (4) (2003) 209–230.

[28] G. Monegato, L. Scuderi, Numerical integration of functions with boundary singularities, Journal of Computational and Applied Mathematics 112 (1-2) (1999) 201–214.

[29] I. Babuska, F. Ihlenburg, E.T. Paik, S.A. Sauter, A Generalized Finite Element Method for solving the Helmholtz equation in two dimensions with minimal pollution, Computer Methods in Applied Mechanics and Engineering 128 (3-4) (1995) 325–359.

[30] J. Biermann, O. von Estorff, S. Petersen, C. Wenterodt, Higher order finite and infinite elements for the solution of Helmholtz problems, Computer Methods in Applied Mechanics and Engineering 198 (13–14) (2009) 1171 – 1188.